Compressible-Gas Invasion into Liquid-Saturated Porous Media: Application to Polymer-Electrolyte-Membrane Electrolyzers

ChungHyuk Lee,[1] Benzhong Zhao,[1,†] Rami Abouatallah,[2] Rainey Wang,[2] and Aimy Bazylak[1,*]

[1] *University of Toronto, 5 King's College Road, Toronto, Ontario, Canada M5S 3G8*

[2] *Hydrogenics Corporation, 220 Admiral Boulevard, Mississauga, Ontario, Canada L5T 2N6*

(Received 24 November 2018; revised manuscript received 19 March 2019; published 10 May 2019)

Understanding gas transport in liquid-saturated porous media is crucial for reducing mass transport-related inefficiencies in polymer-electrolyte-membrane (PEM) electrolyzers. While incompressible fluid-fluid displacement in porous media has been studied extensively, transport behavior with high compressibility effects remains poorly understood. Here, we investigate the impact of compressibility on gas transport in porous media via experiments in patterned micromodels. Macroscopically, we find that the displacement pattern follows the classical transition from capillary to viscous fingering as capillary number increases, despite the compressed state of the injected gas. Microscopically (i.e., pore scale), we find that the displacement occurs via discrete bursts in the form of Haines jumps. We demonstrate that in the presence of compressibility, the pore throat size exerts fundamental control over the burst velocity. Furthermore, we show that the inclusion of a thin, low-porosity region with small pore throats at the inlet of the micromodel increases the burst velocity of gas into the bulk of the micromodel, leading to significantly reduced gas saturation in the bulk. Our work provides a mechanistic explanation of the previously reported performance improvement due to the addition of microporous layers in PEM electrolyzers.

DOI: 10.1103/PhysRevApplied.11.054029

I. INTRODUCTION

Despite significant progress in renewable energy technologies, such as solar and wind in the past decade, the intermittency of such energy sources remains as a major barrier to the establishment of a sustainable energy infrastructure [1,2]. Therefore, it is essential that the excess energy from these renewable sources be stored during periods of high energy generation, which can then be used during periods of low energy generation. The polymer-electrolyte-membrane (PEM) electrolyzer is a promising technology for storing renewable energy in the form of hydrogen, due to its rapid system response and the capability to operate under a wide range of input power [3,4]. However, the energy efficiency of PEM electrolyzers must improve significantly to become economically viable at large scales [5].

To become commercially viable on a large scale, PEM electrolyzers need to operate at high operating temperatures and current densities [6]. Specifically, a higher operating temperature improves the efficiency of the electrolysis and a higher current density allows for a reduction in cost of electrolyzer stacks. A particularly challenging issue associated with such operating conditions is the accumulation of oxygen gas bubbles at the anode porous transport layer (PTL), which hinders the reactant (i.e., liquid water) from reaching the catalyst sites, greatly reducing the efficiency of PEM electrolyzers [7,8]. Hence, understanding gas transport through the PTL is an important first step in designing more efficient PEM electrolyzers.

The displacement of liquid water by the oxygen gas in the PTL can be characterized as viscously unfavorable drainage flow, since water is more viscous than the oxygen gas and more wetting to the titanium-based PTL substrate [9]. Viscously unfavorable drainage flow in porous media has been studied extensively [10–12] and this particular type of flow has been shown to exhibit unique flow patterns that include capillary fingering and viscous fingering. Thanks to these pioneering studies, we now have a fairly good understanding of the transition between capillary fingering and viscous fingering, which is controlled by the capillary number (Ca)—a measure of the relative strength between viscous forces and capillary forces. Capillary fingering occurs at low Ca and is characterized by a fractal-like displacement pattern that encompasses pockets of trapped viscous defending fluid [13,14]. Additionally, capillary fingering grows in an intermittent manner that involves fast displacement events known as "Haines jumps" [14–16]. Viscous fingering occurs at high Ca and is characterized by a ramified displacement pattern

*abazylak@mie.utoronto.ca

†Present address: McMaster University, 1280 Main Street West, Hamilton, Ontario, Canada L8S 4L7.

[11,17,18]. However, most of the experimental studies of drainage in porous media to date have been limited to the incompressible limit. Experimentally, incompressible drainage flow is achieved via using incompressible fluid pairs [19,20] or by withdrawing a wetting liquid from a porous medium connected to the atmosphere [14,15,21], such that air displaces the liquid at atmospheric pressure.

In contrast with the wealth of observations in incompressible fluid-fluid displacements, drainage flow with high compressibility effects remains relatively unexplored. Compressibility of the invading phase adds complexity to the underlying physics of the displacement, since the motion of compressible fluids is unsteady and impulsive. We expect this flow regime to be highly relevant in PEM electrolyzers operating at atmospheric conditions, since the produced oxygen gas is highly susceptible to compression. The anode side of PEM electrolyzers is often kept at atmospheric pressure conditions for safety reasons and to reduce the operating cost [4,22,23].

Here, we use patterned micromodels to study the impact of compressibility on gas transport in the porous transport layer of PEM electrolyzers. We image the invasion experiments in high spatial and temporal resolutions, which allows us to elucidate the flow behavior at the pore scale and its impact on the macroscopic displacement pattern. We observe the classical transition from capillary fingering to viscous fingering in our micromodel, despite the highly compressed state of the invading gas. Although the macroscopic displacement patterns of the invading gas closely resemble those of incompressible fluid-fluid displacements, the microscopic (i.e., pore-scale) dynamics of the invasion is strongly controlled by compressibility. Specifically, we find that the interface velocity associated with such bursts increases with decreasing pore throat size. This key insight allows us to design a micromodel geometry with a dual porosity distribution, which is shown to reduce the gas saturation in the bulk of the micromodel. Our findings support the inclusion of a microporous layer (MPL) in PEM electrolyzer PTLs for more efficient oxygen gas removal.

II. EXPERIMENTAL SETUP

We use micromodels to study the impact of compressibility on gas transport in the PTL of PEM electrolyzers. The micromodels are quasi-two-dimensional (2D) flow cells patterned with cylindrical posts with uniform diameter $D = 100$ μm and height $h = 90$ μm to simulate the solid grains of the PTL [Fig. 1(a)]. The micromodel geometry is generated using a 2D stochastic pore network generation algorithm [24] that mimics the characteristic pore structure of fibrous PTLs [25,26]. Specifically, the algorithm pseudorandomly places cylindrical posts that represent fibers of the PTL in a rectangular domain until the network reaches the prescribed porosity $\phi = 0.8$ and

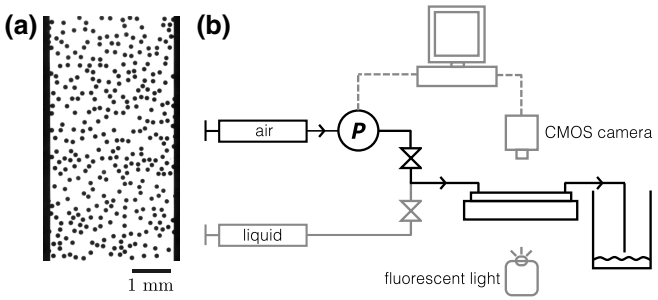

FIG. 1. Experimental setup. (a) We design and fabricate a micromodel patterned with circular discs to simulate the structure of the porous transport layer (PTL). (b) We perform constant-rate injection of air into a porous micromodel filled with fluorescein-dyed ethanol. A pressure sensor records the injection pressure throughout the experiment. We image the displacement of ethanol by air in high spatial and temporal resolution with an optical CMOS camera.

mean pore diameter $d_{\text{pore}} = 90$ μm. The micromodels are fabricated with polydimethylsiloxane (PDMS) via a soft photolithography technique [27]. Two PDMS slabs are prepared for the micromodel: a patterned PDMS slab with the generated pore network features and a flat PDMS slab to seal the bottom of the features. The height of the posts are measured using an optical profilometer (Bruker Contour GT-K from Bruker Optics Inc.) and the measured heights are 0.09 mm. For the detailed fabrication procedure, the readers are directed to Appendix A.

To perform an experiment, we first fully saturate the flow cell with ethanol ($\mu_{\text{liq}} = 1.074$ mPa s) that is dyed with fluorescein (0.001 M). We use ethanol since its wettability to PDMS in the presence of air is similar to that of water to titanium in the presence of air ($\theta = 50^\circ$) [8]. The ambient ethanol is displaced by air ($\mu_{\text{gas}} = 0.018$ mPa s) at constant volumetric flow rate Q [Fig. 1(b)]. The viscosity ratio between these two fluids is $M = \mu_{\text{liq}}/\mu_{\text{gas}} = 59$. We characterize the relative significance of viscous forces relative to capillary forces using the classical macroscopic capillary number:

$$\text{Ca} = \frac{v\mu_{\text{liq}}}{\gamma \cos\theta}, \tag{1}$$

where v is the imposed macroscopic displacement velocity, $\gamma = 22$ mN/m is the interfacial tension between ethanol and air, and $\theta = 50^\circ$ is the contact angle of ethanol on PDMS in the presence of air. The macroscopic displacement velocity is defined as $v = Q/A\phi$, where A and ϕ are the cross-sectional area and the average porosity of the micromodel, respectively. By varying the injection rate from 1.8 to 383 μL/min, we achieve capillary numbers that span over 2 orders of magnitude ($1.3 \times 10^{-6} \leq \text{Ca} \leq 2.5 \times 10^{-4}$). We visualize the experiments with an

optical microscope (DMI 3000 B, Leica) with a fluorescent light source (X-Cite Series 120 Q, Excelitas Technologies). Images are captured at 20 to 250 frames per second (depending on the injection rate) using a complementary metal-oxide-semiconductor (CMOS) camera (C11440-22CU, Hamamatsu) with a spatial resolution of 9.4 μm/pixel. A pressure transducer (PX309-005G5V, Omega Inc.) is used to monitor the air pressure evolution throughout the experiment.

III. EXPERIMENTAL RESULTS

A. Transition from capillary fingering to viscous fingering

We measure the evolution of the injection pressure and observe that the gas pressure increases linearly over time for all injections [Fig. 2(a)]. These pressure data are distinct from previously reported pressure measurements associated with viscously unfavorable drainage flow in incompressible systems: the injection pressure in the capillary fingering regime (i.e., small Ca) is known to oscillate around a characteristic capillary pressure [14,21] and the injection pressure in the viscous fingering regime (i.e., large Ca) has been observed to decrease as the invading fluid nears the outlet [20].

To elucidate the mechanistic cause of the observed pressure increase in our experiments, we quantify the volume of the injected air in the micromodel via image analysis. We find that the rate at which the air volume increases is significantly lower than the prescribed volumetric injection rate (i.e., $V < V_p$). The effect of compressibility is most pronounced at low Ca, where compression-induced pressurization of the injected air is required to overcome the capillary entry pressure. This invasion mechanism is manifested in the plateau regions of the cumulative volume curve, which is followed by a fast ramp-up in volume [Fig. 2(b)]. While volume expansion due to pore invasion is significant at the scale of the micromodel, it is negligible compared to volume compression due to injection, such that the pressure continues to increase [Fig. 2(a)].

Despite the highly compressed state of the injected gas, we observe invasion patterns [Fig. 3(a)] that closely resemble the classical capillary-number-dependent transition from capillary fingering to viscous fingering obtained from incompressible fluid-fluid displacement experiments. We quantify the invasion patterns at breakthrough by measuring their fractal dimension D_f in 2D via the box-counting method [Fig. 3(b)]. At low injection rates, the fractal dimension remains relatively constant ($1.8 \leq D_f \leq 1.81$) over an order of magnitude change in capillary number ($2.5 \times 10^{-6} \leq \mathrm{Ca} \leq 2.5 \times 10^{-5}$). These measurements are in close agreement with the well-established D_f values for capillary fingering for incompressible fluid-fluid displacement [13,28]. As the injection rate increases,

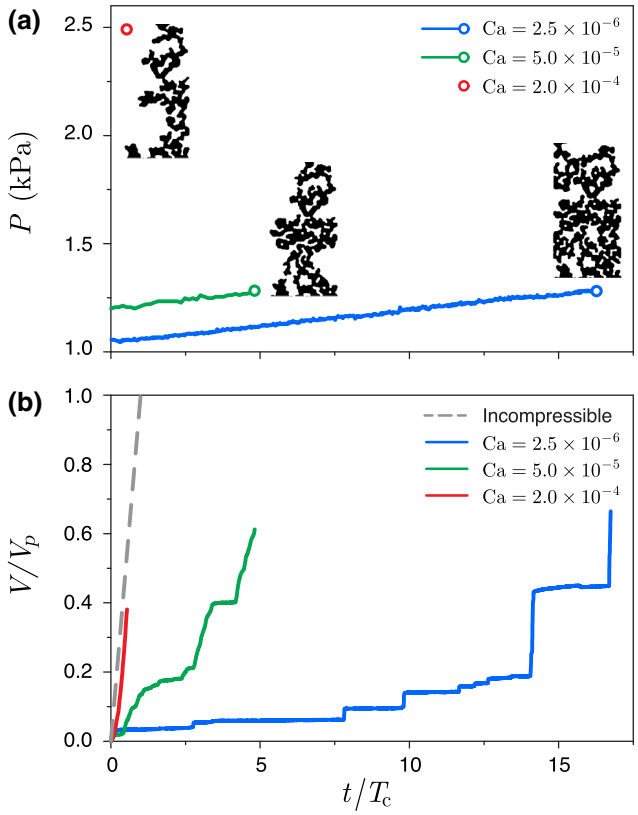

FIG. 2. (a) Evolution of the injection pressure in the gas phase at $\mathrm{Ca} = 2.5 \times 10^{-6}$ (blue line), $\mathrm{Ca} = 5.0 \times 10^{-5}$ (green line), and $\mathrm{Ca} = 2.0 \times 10^{-4}$ (red line). The open circles indicate breakthrough, which is when the invading gas escapes the boundary of the micromodel. The injection pressure increases with time in the experiments due to the compression of the gas phase. (b) Volume evolution of the injected air in the micromodel. We nondimensionalize the total injected volume V by the pore volume V_p and time by the characteristic time $T_c = V_p/Q$. The volume evolution curves fall below the theoretical volume evolution curve of incompressible fluid injection (gray dashed line), which indicates gas compression during injection. Additionally, gas invasion at the low Ca (blue solid line) advances in sudden bursts, followed by long quiescent periods. See Video 1 in Appendix B.

however, the displacement pattern becomes increasingly ramified, a trend that is accompanied by decreasing D_f values. Specifically, we find $D_f \to 1.76$ as $\mathrm{Ca} \to 2.0 \times 10^{-4}$ [Fig. 3(b)]. These measurements are also consistent with existing D_f values for the transition from capillary fingering to viscous fingering in incompressible systems [28,29]. The D_f measurements demonstrate that the macroscopic invasion pattern of our system is controlled by the relative importance between capillary forces and viscous forces, despite the highly compressed state of the invading gas.

We further quantify the displacement process by measuring the breakthrough gas saturation S_{bt}, whose dependence on Ca follows a similar trend to that of D_f

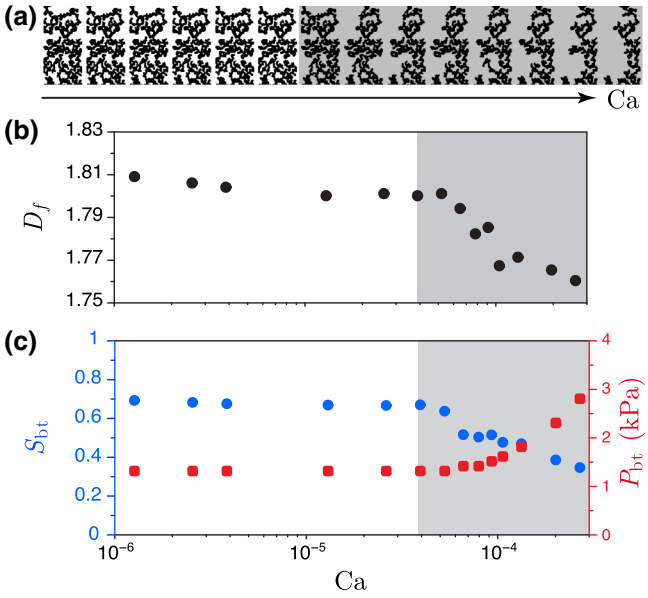

FIG. 3. (a) The displacement patterns of gas (black) invading ethanol transition from capillary fingering (white background) to viscous fingering (gray background) with increasing capillary number. (b) The corresponding fractal dimension (D_f) measurements ($1.81 \leq D_f \leq 1.76$) are in agreement with the classical values that correspond to the transition between capillary fingering and viscous fingering for incompressible flows. (c) Breakthrough gas saturation (blue circles) decreases as the invasion transitions from capillary fingering to viscous fingering with increasing Ca. The decrease in saturation is accompanied by an increase in the breakthrough gas pressure (red squares).

[Fig. 3(c)]. At a low injection rate, the breakthrough gas saturation remains constant ($S_{bt} \approx 0.7$) over an order of magnitude change in capillary number ($2.5 \times 10^{-6} \leq \mathrm{Ca} \leq 2.5 \times 10^{-5}$). The constant S_{bt} over this range of Ca is consistent with the capillary fingering regime, where each invasion event occurs at the pore throat with the lowest entry capillary pressure. This capillary pressure-limited mechanism leads to an invasion sequence that is determined solely by the pore structure of the micromodel, as described by the classical invasion percolation algorithm [13,30]. Furthermore, this displacement process is evidenced by the constant breakthrough gas pressure $P_{bt} = 0.33$ kPa for $2.5 \times 10^{-6} \leq \mathrm{Ca} \leq 2.5 \times 10^{-5}$, which corresponds to the capillary entry pressure associated with the last pore throat before breakthrough [Fig. 3(c)]. As the displacement transitions from capillary fingering to viscous fingering at higher injection rates, S_{bt} decreases with increasing Ca. The decrease in S_{bt} is accompanied by an increase in the breakthrough pressure, which reflects the growing significance of viscous forces.

B. Local invasion velocities

Our analyses so far have demonstrated that the macroscopic displacement of a liquid phase by a compressed gas phase in porous media is similar to that of incompressible systems, as indicated by the invasion patterns, the fractal dimensions, and the trend in breakthrough gas saturation and injection pressure. However, these macroscopic observations do not reveal information about the displacement mechanisms at the microscopic scale (i.e., pore scale). It is well known that the macroscopically smooth drainage flow at low Ca results from a series of discrete bursts at the pore scale, commonly known as "Haines jumps" [31]. Crucially, these pore-scale jumps occur at interfacial velocities much faster than the macroscopic displacement velocity [16,19,32]. To gain insight into the pore-scale displacement process of our experiments, we track interface movement by comparing the fluid-fluid interface between two consecutive images. The local interfacial velocities v^* are given by the Euclidean displacement of each interface pixel divided by the time interval δt between consecutive images. We analyze the maximum instantaneous interfacial velocity v^*_{max} as a function of time and find that in the capillary finger regime, the evolution of the maximum interfacial velocity is characterized by long periods of slow creeping flow, interspersed with short bursts of fast Haines jumps (Fig. 4).

The discrete Haines jumps can be characterized by the local capillary number (Ca^*) and the local Reynolds number (Re^*). Specifically, $\mathrm{Ca}^* = \mu v^*_{max}/\gamma \cos\theta$ characterizes the ratio of viscous forces to capillary forces during a single pore throat invasion, in contrast to Ca, which is a

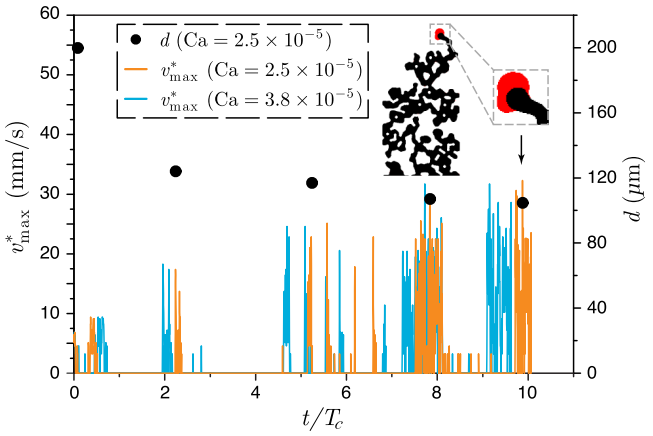

FIG. 4. Evolution of the maximum local interfacial velocity v^*_{max} at $\mathrm{Ca} = 2.5 \times 10^{-5}$ (orange line) and $\mathrm{Ca} = 3.8 \times 10^{-5}$ (blue line). The invasion process is characterized by long periods of slow creeping flow ($v^*_{max} = 0$), interspersed with short bursts of fast Haines jumps. The v^*_{max} of the Haines jump increases as the invasion progresses, which corresponds to a decrease in the pore throat diameter d (black circles) where the jump occurs. We find the pore structure exerts fundamental control over the v^*_{max} associated with interface jumps, as demonstrated by the remarkably similar v^*_{max} between experiments conducted at $\mathrm{Ca} = 2.5 \times 10^{-5}$ and $\mathrm{Ca} = 3.8 \times 10^{-5}$.

macroscopic capillary number based on the imposed flow rate on the micromodel. Additionally, $\mathrm{Re}^* = \rho v^*_{\max} d/\mu$ characterizes the ratio of inertial forces to viscous forces during a single pore throat invasion, where $\rho = 789\ \mathrm{kg/m^3}$ is the density of ethanol at 20 °C. We find the maximum local capillary number $\mathrm{Ca}^* = 1.5 \times 10^{-3}$ is almost 2 orders of magnitude larger than the macroscopic capillary number $\mathrm{Ca} = 2.5 \times 10^{-5}$, since the interfacial velocity of the jump ($v^*_{\max} = 32$ mm/s) is much larger than the imposed displacement velocity ($v = 0.31$ mm/s). The large interfacial velocity is additionally associated with significant inertial effects, as reflected by the local Reynolds number $\mathrm{Re}^* = 2.2$.

While $v^*_{\max}$ of the Haines jumps is always significantly larger than the macroscopic displacement velocity, surprisingly, the magnitude of $v^*_{\max}$ increases with each subsequent jump as the invasion progresses (Fig. 4). To elucidate the mechanistic cause of the observed increase in $v^*_{\max}$, we refer to the classical experiments of Gauglitz and Radke [33], who studied the dynamics of Haines jumps for compressible-gas bubbles in constricted capillary tubes. In particular, they demonstrated that the compressibility-driven jump velocity is predominantly controlled by the size of the constriction (cf. pore throat size) and that decreasing the size of the constriction increases the velocity of the jump. We quantify the pore throat size d associated with each burst and find that it is indeed inversely related to the jump velocity (Fig. 4). This observation indicates that the jump velocity in the capillary fingering regime is controlled by the structure of the porous media and independent of the imposed displacement rate, since the invading gas encounters the same sequence of pore throats following the invasion percolation process. Remarkably, we find striking similarities in the interfacial velocities observed at $\mathrm{Ca} = 2.5 \times 10^{-5}$ and $\mathrm{Ca} = 3.8 \times 10^{-5}$ (Fig. 4). Our results extend the findings of Gauglitz and Radke [33] to a porous medium: the interface velocity of compressible-gas invasion in the capillary fingering regime is mainly controlled by the pore throat size.

C. Microporous layer promotes gas transport

Our results thus far demonstrate that at low Ca, both the statics (i.e., invasion sequence) and the dynamics (i.e., interfacial jumps) of compression-driven gas invasion are controlled by the structure of the porous media. These observations could potentially be exploited to tailor the effectiveness of gas transport. In fact, recent studies have shown that the inclusion of a microporous layer in the anode PTL of PEM electrolyzers results in lower overpotential at high current densities due to improved mass transport [34,35]. The MPLs reported in these studies are thin, porous titanium coatings with smaller porosities (approximately 0.1) and pore sizes (approximately 1 μm) compared to the porosities (approximately 0.5) and pore sizes (approximately 10 μm) of traditional PTLs [36–38].

Inspired by these findings, we design a heterogeneous micromodel to study the impact of MPLs on gas transport [Fig. 5(a)]. The geometry of the heterogeneous micromodel is based on published microcomputed tomography imaging data of fibrous PTLs with MPLs [26]. Specifically, the bottom third of the heterogeneous micromodel is assigned a lower porosity ($\phi = 0.73$) and smaller mean pore throat size ($d \approx 35\ \mu$m) than the upper two thirds of the micromodel ($\phi = 0.85$, $d \approx 60\ \mu$m) to mimic the inclusion of a MPL in the PTL. At $\mathrm{Ca} = 2.5 \times 10^{-5}$, the invading gas progresses through the MPL region of the micromodel in a capillary-fingeringlike manner, as characterized by fast interfacial jumps followed by long periods of quiescence [Figs. 5(b)–5(c)]. The quiescent period in the MPL is particularly prolonged, since a greater compression

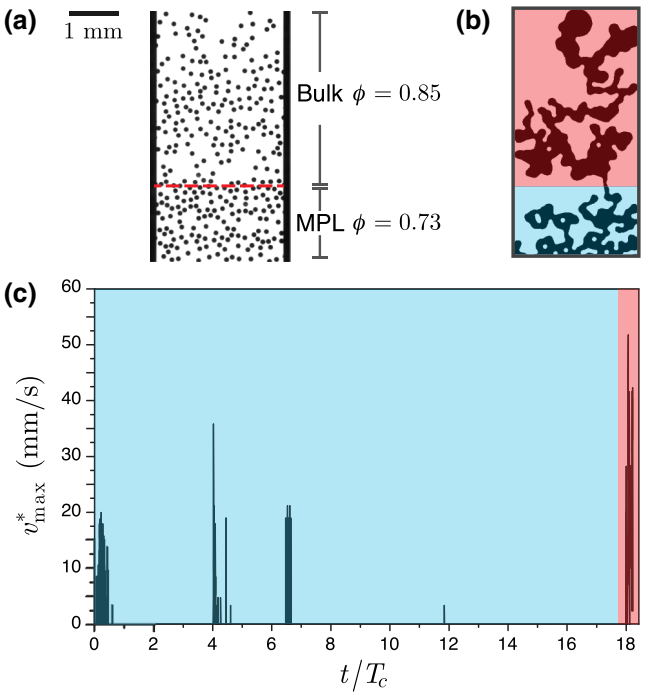

FIG. 5. (a) We design and fabricate a heterogeneous micromodel to investigate the impact of MPL on gas transport. The red dashed line separates the MPL region ($\phi = 0.73$, $d \approx 50\ \mu$m) from the bulk PTL region ($\phi = 0.85$, $d \approx 120\ \mu$m). (b) The breakthrough displacement pattern in the heterogeneous micromodel at $\mathrm{Ca} = 2.5 \times 10^{-5}$. (c) Evolution of the maximum interfacial velocity $v^*_{\max}$ for the experiment shown in (b). The invasion in the MPL region of the micromodel (shaded blue) occurs in a capillary-fingeringlike manner, as characterized by fast interfacial jumps followed by long periods of quiescence. In particular, the gas exits the MPL region in a powerful burst (shaded red), leading to near instantaneous discharge through the rest of the micromodel. In contrast to the intertmittent invasion behavior in the MPL, the invasion process in the bulk of the micromodel occurs in a continuous fashion. See Video 2 in Appendix B.

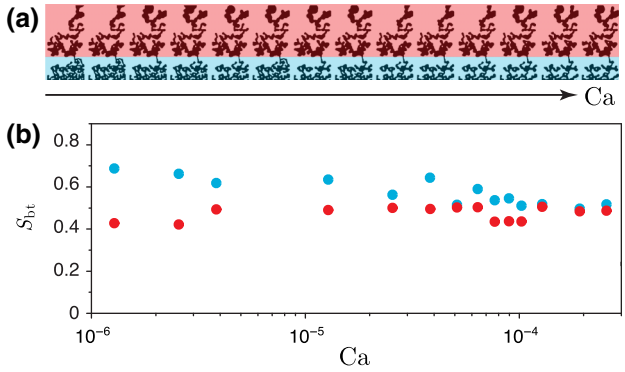

FIG. 6. (a) Displacement patterns of gas invading ethanol in the heterogeneous micromodel. The MPL region of the micromodel (shaded blue) exerts fundamental control over the invasion process, which results in strikingly similar displacement patterns (a) and near-constant breakthrough gas saturation (b) in the bulk of the micromodel (red circles), despite over 2 orders of magnitude change in the capillary number. Additionally, the MPL region of the heterogeneous micromodel exhibits the same breakthrough gas saturation (blue circles) as that of the homogeneous micromodel [Fig. 3(c)] across a wide range of capillary numbers.

of the gas phase is required to overcome the higher capillary pressure associated with the smaller pore throats. As a result, we observe a powerful burst with $v^*_{max} = 52$ mm/s as the invading gas escapes the MPL region. Remarkably, this burst event leads to a near instantaneous discharge of the invading gas through the micromodel [Fig. 5(c); Video 2 in Appendix B.

In contrast to the capillary-number-controlled transition from capillary fingering to viscous fingering in the uniform micromodel [Fig. 3(a)], the displacement pattern in the bulk of the heterogeneous micromodel (i.e., outside of the MPL) is intentionally insensitive to Ca (Fig. 6). This observation is confirmed quantitatively by the constant breakthrough gas saturation in the bulk of the micromodel ($S^{bulk}_{bt} \approx 0.5$) over a 2 orders of magnitude change in Ca. While the breakthrough gas saturation in the MPL region of the micromodel S^{MPL}_{bt} is similar to that observed in the entire homogeneous micromodel [Fig. 6(b)], the MPL enforces a low breakthrough gas saturation in the bulk of the PTL. Specifically, these results demonstrate that the small pore throats in the MPL exert a fundamental control on gas transport in the PTL, leading to a viscous fingering-type displacement in the PTL bulk over a wide range of Ca. Our findings echo the recent demonstrations of pore geometry control in *suppressing* viscous fingering in structured porous media [39]. Here, we show that the inclusion of a MPL in the PTL *promotes* viscous fingering, which results in lower gas saturations in the PTL bulk. The reduced gas saturation in the PTL enables more efficient reactant delivery and, thus, better-performing PEM electrolyzers.

IV. CONCLUSIONS

We systematically investigate the impact of compressibility on gas transport in porous media via experiments in patterned micromodels. This problem is highly relevant to the mass transport phenomenon in PEM electrolyzers. Specifically, the anode reaction of a PEM electrolyzer produces oxygen gas bubbles, whose accumulation in the PTL hinders liquid water from reaching the catalyst site, greatly reducing the efficiency of the electrolyzer. Hence, a clear understanding of gas transport through the PTL is essential for the design of more efficient PEM electrolyzers, but the vast majority of previous work on fluid-fluid displacement in porous media has focused on incompressible systems.

Our experiments show that despite the highly compressed state of the invading gas, the macroscopic displacement patterns closely resemble the classical transition from capillary fingering toward viscous fingering as the capillary number increases. We support our visual observations by demonstrating the corresponding decreases in the fractal dimensions of the displacement patterns and the breakthrough gas saturations over two orders of magnitude increase in Ca (Fig. 3). We further show that within the capillary fingering regime, the invasion mechanism at the microscopic scale (i.e., pore scale) is dominated by discrete bursts in the form of Haines jumps. The pore-scale interfacial velocity is predominantly controlled by the pore throat size where the Haines jump occurs and the smaller pore throats are associated with higher interfacial velocities (Fig. 4). An important implication of our results is that the structure of the porous media may be tailored to exploit the dynamics of compressible gas invasion in liquid-filled porous media to promote more efficient gas transport. Indeed, we find that the inclusion of a low-porosity region with small pore throats near the inlet of the micromodel results in lower breakthrough gas saturations in the bulk of the micromodel, despite over 2 orders of magnitude change in Ca [Fig. 6(b)]. Our findings support the inclusion of a microporous layer in the PTL of PEM electrolyzers for improved mass transport.

ACKNOWLEDGMENTS

Financial support from the Natural Sciences and Engineering Research Council of Canada (NSERC), the NSERC Collaborative Research and Training Experience Program (CREATE) in Distributed Generation for Remote Communities, the Canada Research Chairs Program, and the Ontario Ministry of Research and Innovation Early Researcher Award are gratefully acknowledged. Also, the authors gratefully acknowledge the financial support of the International Cooperation and Exchange of the National Natural Science Foundation of China (Grant No. 51620105011). Graduate scholarships to C.H.L. from the Pierre Rivard Hydrogenics Graduate Fellowship, Bert Wasmund Graduate Fellowships in Sustainable Energy

Research, C.W. Bowman Graduate Scholarship, William Dunbar Memorial Fellowship in Mechanical Engineering, and the Ontario Graduate Scholarship are gratefully acknowledged.

APPENDIX A: MICROMODEL FABRICATION

The generated pore networks are fabricated via soft lithography and housed in straight microchannels. The pore networks are printed on a 5-in. soda lime photomask using a mask writer (uPG 501, Heidelberg). The printed photomask is post-treated with a three-step etching process that included the follow steps: (i) etching in a 1:10 volume ratio of AZ 400K (MicroChem Corp.) to deionized water; (ii) etching in a chromium etchant (CEP-200, Microchrome Tech.); and (iii) etching in a positive photoresist stripper (PRS-100, Microchrome Tech).

The micromodel fabrication begins with the application of a photoresist (SU8-2050 from MicroChem Corp.) onto a 4-in. silicon wafer (from WaferWorld Inc.) using a spin-coater (Model G3P-8 from Specialty Coating Systems). The spin coating speed of the silicon wafer is set to 500 rpm for 5 s and to 1800 rpm for 30 s. After coating, the wafer is soft-baked on a hot plate at 65 °C for 5 min and at 95 °C for 16 min. The baked wafer is exposed to ultraviolet (UV) light (exposure energy of 230 mJ/cm^2) using a mask aligner (EVG620 from EVG) with the photomask placed on top of the wafer. The wafer is subjected to a postexposure bake on a hot plate, first at 65 °C for 5 min, followed by 95 °C for 9 min. After the bake, the wafer is placed inside a glass dish filled with SU8 developer (from Microchem Corp.) and the dish is stirred on an orbital shaker for 5 min to accelerate the etching process. The etched wafer is washed using isopropanol and hard-baked on a hot plate at 150 °C for 5 min. Finally, the heights of the photoresist features on the wafer (masters for casting the micromodels) are measured using an optical profilometer (Bruker Contour GT-K, Bruker Optics Inc.). The cured photoresist is used to fabricate the micromodels made of PDMS (Sylgard 184m, Dow Corning). Two PDMS parts are prepared for each chip: the PDMS part with the channel features and a PDMS slab to seal the bottom of the channels. PDMS is first mixed with a curing agent with a mass ratio of 10:1 (PDMS to the curing agent), poured onto the master, and degassed for an hour. The PDMS slab is prepared separately on a disposable Petri dish and also degassed for an hour. The two PDMS parts are baked in an oven that is maintained at 60 °C for an hour. After the curing is complete, the two pieces are bonded by treating the surfaces with plasma. The combined pieces are heated in an oven that is maintained at 60 °C for 12 h.

APPENDIX B: EXPERIMENTAL VIDEOS

The videos show gas invasion experiments at Ca = 1:3 × 10^{-4} and Ca = 2:5 × 10^{-5} for the homogeneous micromodel (Video 1) and the heterogeneous micromodel (Video 2).

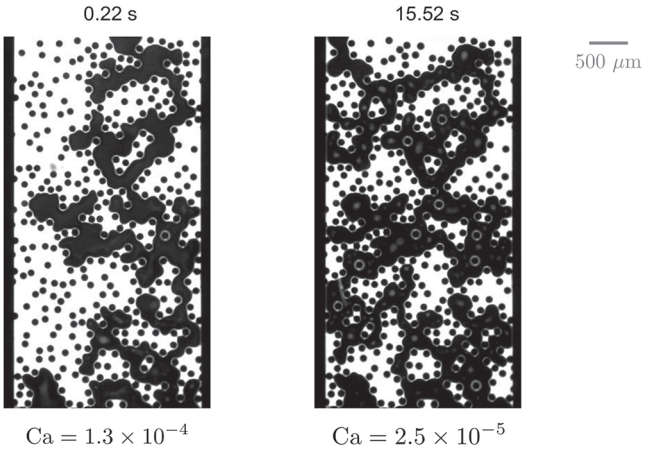

VIDEO 1. Videos of air displacing ethanol in a homogeneous micromodel at Ca = 1.3 × 10^{-4} (left) and Ca = 2.5 × 10^{-5} (right).

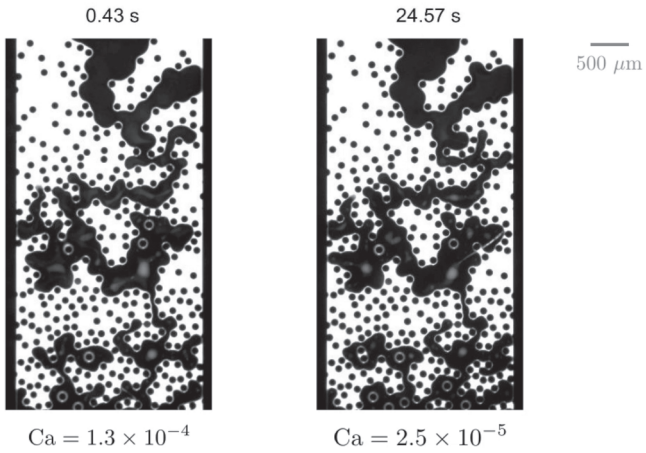

VIDEO 2. Videos of air displacing ethanol in a heterogeneous micromodel (to simulate the inclusion of a MPL in the PTL) at Ca = 1.3 × 10^{-4} (left) and Ca = 2.5 × 10^{-5} (right).

[1] IPCC, *Special Report on Carbon Dioxide Capture and Storage*, edited by B. Metz *et al.* (Cambridge University Press, New York, 2005).

[2] J. A. Turner, A realizable renewable energy future, Science **285**, 687 (1999).

[3] A. Ursúa, L. M. Gandá, and P. Sanchis, Hydrogen production from water electrolysis: Current status and future trends, Proc. IEEE **10**, 410 (2012).

[4] M. Carmo, D. L. Fritz, J. Mergel, and D. Stolten, A comprehensive review on PEM water electrolysis, Int. J. Hydrogen Energy **38**, 4901 (2013).

[5] M. A. Pellow, C. J. M. Emmott, C. J. Barnhart, and S. M. Benson, Hydrogen or batteries for grid storage? A net energy analysis, Energy Environ. Sci. **8**, 1938 (2015).

[6] C. K. Mittelsteadt, PEM electrolysis: Ready for impact, ECS Trans. **69**, 205 (2015).

[7] M. Suermann, T. J. Schmidt, and F. N. Büchi, Investigation of mass transport losses in polymer electrolyte electrolysis cells, ECS Trans. **69**, 1141 (2015).

[8] F. Arbabi, A. Kalantarian, R. Abouatallah, R. Wang, J. S. Wallace, and A. Bazylak, Feasibility study of using microfluidic platforms for visualizing bubble flows in electrolyzer gas diffusion layers, J. Power Sources **258**, 142 (2014).

[9] C. Lee, J. Hinebaugh, R. Banerjee, S. Chevalier, R. Abouatallah, R. Wang, and A. Bazylak, Influence of limiting throat and flow regime on oxygen bubble saturation of polymer electrolyte membrane electrolyzer porous transport layers, Int. J. Hydrogen Energy **42**, 2724 (2017).

[10] L. Paterson, Diffusion-limited Aggregation and Two-fluid Displacements in Porous Media, Phys. Rev. Lett. **52**, 1621 (1984).

[11] K. J. Måløy, J. Feder, and T. Jøssang, Viscous Fingering Fractals in Porous Media, Phys. Rev. Lett. **55**, 2688 (1985).

[12] R. Lenormand, E. Touboul, and C. Zarcone, Numerical models and experiments on immisible displacements in porous media, J. Fluid Mech. **189**, 165 (1988).

[13] R. Lenormand and C. Zarcone, Capillary fingering: Percolation and fractal dimension, Transport Porous Med. **4**, 599 (1989).

[14] K. J. Måløy, L. Furuberg, J. Feder, and T. Jssang, Dynamics of Slow Drainage in Porous Media, Phys. Rev. Lett. **68**, 2161 (1992).

[15] L. Furuberg, K. J. Måløy, and J. Feder, Intermittent behavior in slow drainage, Phys. Rev. E **53**, 966 (1996).

[16] S. Berg, H. Ott, S. A. Klapp, A. Schwing, R. Neiteler, N. Brussee, A. Makurat, L. Leu, F. Enzmann, J. Schwarz, M. Kersten, S. Irvine, and M. Stampanoni, Real-time 3D imaging of Haines jumps in porous media flow, Proc. Natl. Acad. Sci. USA **110**, 3755 (2013).

[17] J.-D. Chen and D. Wilkinson, Pore-scale Viscous Fingering in Porous Media, Phys. Rev. Lett. **55**, 1892 (1985).

[18] G. M. Homsy, Viscous fingering in porous media, Ann. Rev. Fluid Mech. **19**, 271 (1987).

[19] R. T. Armstrong and S. Berg, Interfacial velocities and capillary pressure gradients during haines jumps, Phys. Rev. E **88**, 043010 (2013).

[20] B. Zhao, C. W. MacMinn, and R. Juanes, Wettability control on multiphase flow in patterned microfluidics, Proc. Natl. Acad. Sci. U.S.A. **113**, 10251 (2016).

[21] F. Moebius and D. Or, Pore scale dynamics underlying the motion of drainage fronts in porous media, Water Resour. Res. **50**, 8441 (2014).

[22] L. Degiorgis, M. Santerelli, and M. Calí, Hydrogen from renewable energy: A pilot plant for thermal production and mobility, J. Power Sources **171**, 237 (2007).

[23] T. Smolinka, E. T. Ojong, and T. Lickert, *Fundamentals of PEM Water Electrolysis* (CRC Press, Boca Raton, 2015), Chap. 2.

[24] J. Hinebaugh, Z. Fishman, and A. Bazylak, Unstructured pore network modeling with heterogeneous PEMFC GDL porosity distributions, J. Electrochem. Soc. **157**, B1651 (2010).

[25] C. M. Hwang, M. Ishida, H. Ito, T. Maeda, A. Nakano, Y. Hasegawa, N. Yokoi, A. Kato, and T. Yoshida, Influence of properties of gas diffusion layers on the performance of polymer electrolyte-based unitized reversible fuel cells, Int. J. Hydrogen Energy **36**, 1740 (2011).

[26] L. Zielke, A. Fallisch, N. Paust, R. Zengerle, and S. Thiele, Tomography based screening of flow field/current collector combinations for PEM water electrolysis, RSC Adv. **4**, 58888 (2014).

[27] Y. Xia and G. M. Whitesides, Soft lithography, Annu. Rev. Mater. Sci. **28**, 153 (1998).

[28] J. F. Fernandez, R. Rangel, and J. Rivero, Crossover Length from Invasion Percolation to Piffusion-limited Aggregation in Porous Media, Phys. Rev. Lett. **67**, 2958 (1991).

[29] M. Ferer, C. Ji, G. S. Bromhal, J. Cook, G. Ahmadi, and D. H. Smith, Crossover from Capillary Fingering to Viscous Fingering for Immiscible Unstable Plow: Experiment and Modeling, Phys. Rev. E **70**, 016303 (2004).

[30] D. Wilkinson and J. Willemsen, Invasion percolation: A new form of percolation theory, J. Phys. A **16**, 3365 (1983).

[31] W. B. Haines, Studies in the physical properties of soil. V. The hysteresis effect in capillary properties, and the modes of moisture distribution associated therewith, J. Agric. Sci. **20**, 97 (1930).

[32] F. Moebius and D. Or, Interfacial jumps and pressure bursts during fluid displacement in interacting irregular capillaries, J. Colloid Interface Sci. **377**, 406 (2012).

[33] P. A. Gauglitz and C. J. Radke, Dynamics of haines jumps for compressible bubbles in constricted capillaries, AlChE J. **35**, 230 (1989), cited By :19.

[34] P. Lettenmeier, S. Kolb, F. Burggraf, A. S. Gago, and K. A. Friedrich, Towards developing a backing layer for proton exchange membrane electrolyzers, J. Power Sources **311**, 153 (2016).

[35] P. Lettenmeier, S. Kolb, N. Sata, A. Fallisch, L. Zielke, S. Thiele, A. S. Gago, and K. A. Friedrich, Comprehensive investigation of novel pore-graded gas diffusion layers for high-performance and cost-effective proton exchange membrane electrolyzers, Energy Environ. Sci. **10**, 2521 (2017).

[36] S. A. Grigoriev, P. Millet, S. A. Volobuev, and V. N. Fateev, Optimization of porous current collectors for PEM water electrolysers, Int. J. Hydrogen Energy **34**, 4968 (2009).

[37] H. Ito, T. Maeda, A. Nakano, C. M. Hwang, M. Ishida, A. Kato, and T. Yoshida, Experimental study on porous current collectors of PEM electrolyzers, Int. J. Hydrogen Energy **37**, 7418 (2012).

[38] J. K. Lee and A. Bazylak, Stochastic generation of sintered titanium powder-based porous transport layers in polymer electrolyte membrane electrolyzers and investigation of structural properties, ECS Trans. **80**, 1097 (2017).

[39] H. S. Rabbani, D. Or, Y. Liu, C.-Y. Lai, N. B. Lu, S. S. Datta, H. A. Stone, and N. Shokri, Suppressing viscous fingering in structured porous media, Proc. Natl. Acad. Sci. USA **115**, 4833 (2018).